UC San Diego
UC San Diego Previously Published Works

Title
Plasmons in graphene moiré superlattices

Permalink
https://escholarship.org/uc/item/62v1080w

Journal
Nature Materials, 14(12)

ISSN
1476-1122

Authors
Ni, GX
Wang, H
Wu, JS
et al.

Publication Date
2015-12-01

DOI
10.1038/nmat4425

Peer reviewed

Plasmons in graphene moiré superlattices

G. X. Ni[1,2], H. Wang[3], J. S. Wu[2], Z. Fei[2], M. D. Goldflam[2], F. Keilmann[4], B. Özyilmaz[1], A. H. Castro Neto[1], X. M. Xie[3], M. M. Fogler[2] and D. N. Basov[2]*

Moiré patterns are periodic superlattice structures that appear when two crystals with a minor lattice mismatch are superimposed. A prominent recent example is that of monolayer graphene placed on a crystal of hexagonal boron nitride. As a result of the moiré pattern superlattice created by this stacking, the electronic band structure of graphene is radically altered, acquiring satellite sub-Dirac cones at the superlattice zone boundaries. To probe the dynamical response of the moiré graphene, we use infrared (IR) nano-imaging to explore propagation of surface plasmons, collective oscillations of electrons coupled to IR light. We show that interband transitions associated with the superlattice mini-bands in concert with free electrons in the Dirac bands produce two additive contributions to composite IR plasmons in graphene moiré superstructures. This novel form of collective modes is likely to be generic to other forms of moiré-forming superlattices, including van der Waals heterostructures.

The interaction of the nearly matching hexagonal lattices of graphene and hexagonal boron nitride (hBN) results in a quasiperiodic moiré superlattice[1–3]. The consequences are marked: a new set of superlattice Dirac mini-bands emerges in graphene/hBN heterostructures, leading to a rich variety of interesting effects[4–10]. Evidence for the superlattice mini-bands is found in both spectroscopic and transport measurements[1,6,11–14]. The optical conductivity[4,15] and the plasmon dispersion[15] in moiré graphene have been investigated theoretically. An intriguing prediction[15] is that an additional low-frequency plasmon branch may exist in a range of Fermi energies where the partially gapped mini-bands contain small pockets of carriers that are split off from the Dirac bands. However, no experimental study of plasmonic phenomena in moiré-patterned graphene (MPG) has yet been reported. The quest to fully examine these phenomena is exacerbated by the small (sub-μm²) area of typical superlattice domains that often occur in the immediate proximity of plain graphene (Fig. 1). To alleviate this problem, we made use of the propagating surface plasmon polariton waves launched in the setting of scattering-type scanning near-field optical microscopy (s-SNOM) measurements, thereby enabling experimental access to the electronic band structure and electron–hole excitations of the nanoscale moiré-patterned domains in graphene. Our analysis of plasmonic real-space fringes reveals that bound electrons in the superlattice mini-bands create novel collective characteristics in moiré graphene.

We have carried out nano-IR imaging of Dirac plasmons at UCSD by means of the s-SNOM apparatus (Fig. 1a; see Methods). In this instrument a metallized tip (antenna) of an atomic force microscope (AFM) with curvature radius ∼25 nm was illuminated by IR light, generating strong enhancement of the electric field underneath the tip. This antenna-based nano-IR set-up circumvents the momentum mismatch between light and surface plasmons in graphene[16], allowing us to launch plasmonic waves of wavelength λ_p. These waves propagate radially outwards from the tip and form plasmon fringes with a period of $\lambda_p/2$ owing to the interference between tip-launched and edge-reflected plasmon waves[16,17]. Together,

the wavelength of the plasmonic fringes, the rate at which plasmonic oscillations decay in the interior of the sample, and the amplitude of the overall nano-IR scattering signal contain complete information on the complex conductivity of the graphene layer at the frequency of the IR probe beam ω.
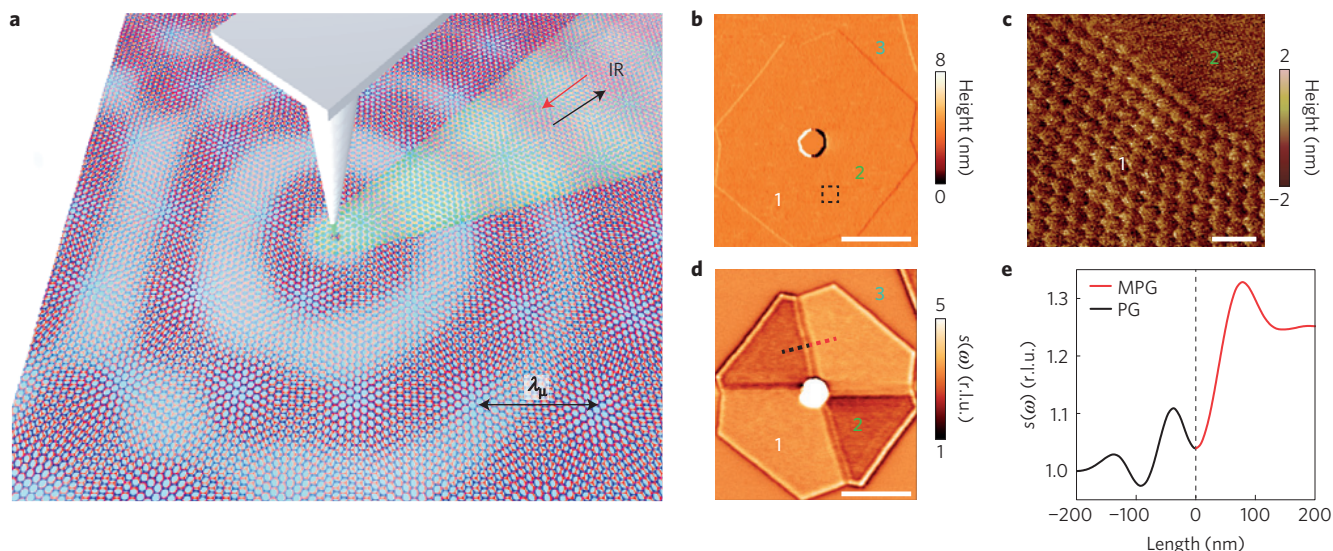
Our graphene microcrystals were grown by means of catalyst-free epitaxial synthesis on top of hBN/quartz[18–20] (see Methods). The key advantage of this synthesis approach over the commonly used dry transfer method[1,11–14] is that graphene microcrystals can be naturally aligned with respect to the hBN lattice, forming MPG with a wavelength $\lambda_{ll} \sim 14$ nm (Fig. 1b,c). Moreover, our approach yields high-quality graphene flakes free of the polymer residuals, bubbles or wrinkles that often plague structures fabricated using alternative methods.

In Fig. 1d, we show typical nano-IR imaging data. Here we plot raster-scanned images of the normalized back scattering amplitude signal $s(\omega)$ at a selected IR frequency $\omega = 890$ cm⁻¹. The MPG regions are directly adjacent to plain (free of superlattice effects) graphene: a virtue that has allowed us to examine the impact of the moiré superlattice in the same microcrystal. These two adjacent regions of a single microcrystal share an identical environment, assuring that the carrier density (n) due to the unintentional doping is uniform through the entire microcrystal[21,22]. The most prominent aspect of the images in Fig. 1d is that the magnitude of the scattering amplitude in MPG regions is enhanced relative to plain graphene (Fig. 1e). Furthermore, every boundary of the sample in Fig. 1d prompts periodic oscillations of the nano-IR signal. These oscillations are signatures of plasmonic reflections that occur at sample edges and at the borders of regions with different complex conductivity $\sigma(\omega) = \sigma_1(\omega) + i\sigma_2(\omega)$ (ref. 23). Therefore, the observed plasmonic reflections are consistent with the notion of dissimilar values of $\sigma(\omega)$ in MPG and plain graphene.

The nano-IR data in Fig. 1d give a rich insight into the electronic processes in moiré superlattices that ultimately govern plasmon propagation and reflection in this system. It is therefore instructive to closely examine the line-profiles along the direction normal to

Figure 1 | AFM and plasmon nano-imaging with s-SNOM. a, Schematic of the nano-IR imaging set-up. **b**, AFM topography image of a G/hBN sample with both a moiré-patterned (regime 1) and a non-patterned regime (regime 2). Regime 3 corresponds to the bare hBN. **c**, A higher-resolution image (friction-AFM) at the boundary between the moiré-patterned and plain graphene, as marked by the dashed square in **b**. The superstructure in regime 1 exhibits hexagonal symmetry with lattice constant $\lambda_\mu \sim 14$ nm; whereas regime 2 shows no noticeable variation. **d**, Nano-IR images of the normalized scattering amplitude $s(\omega)$ as introduced in the text. Scale bars, 1 μm (**b,d**); 40 nm (**c**). **e**, Line-profile across the boundary between MPG and plain graphene indicated in **d**. The profiles are averaged over a width of 100 nm.

the sample edges of both MPG and plain graphene for samples with a range of carrier concentrations. In Fig. 2 we show traces obtained by averaging 10^2 such line-profiles from each sample. These data capture the salient trends in the evolution of the plasmonic response, both in the MPG and plain graphene regions, with variation of the carrier density. Even though our structures are not gate-tunable, by exploring a large number of samples with different levels of unintentional doping, we were able to grasp the pertinent effects of carrier density variation. The half-wavelength of the plasmons in Fig. 2 can be approximately determined from the full-width at half-maximum of the dominant fringe; this protocol is validated through numerical modelling, which captures the gross features of the plasmonic line-profiles (see Supplementary Information). This analysis revealed that plasmons in the MPG and plain graphene regions in the same microcrystal are of similar wavelengths. The data series in Fig. 2 shows that the plasmon wavelength for plain graphene varies between approximately 50 nm and 220 nm. The plasmon wavelength is given by $\lambda_p = 2\pi/q_1$, where q_1 is the real part of the complex plasmon wavenumber $q_p = q_1 + iq_2$. The latter is related to the complex conductivity $\sigma(\omega)$ of graphene via[16]:

$$q_p = \frac{i\omega[1 + \epsilon_{sub}(\omega)]}{4\pi\sigma(\omega)} \tag{1}$$

where the effective permittivity of the substrate ϵ_{sub} is the geometric mean of the in- and out-of-plane permittivities[24]. In plain graphene we can approximate $\sigma(\omega)$ using the common Drude model,

$$\sigma(\omega) = \frac{D}{\tau^{-1} - i\omega}, \quad D = \frac{e^2}{\pi\hbar^2}E_F \tag{2}$$

which has two parameters: Drude weight D and relaxation time τ. Combining equations (1) and (2), one finds the well-known linear scaling between λ_p and the Fermi energy E_F:

$$\lambda_p(\omega) = \frac{8\pi e^2 E_F}{\hbar^2\omega^2[1 + \epsilon_{sub}(\omega)]}, \quad E_F = \hbar v_F\sqrt{\pi n} \tag{3}$$

On the basis of equation (3), we conclude that the variation of the carrier density for data in Fig. 2a–f is from $n = 8 \times 10^{11}$ cm^{-2} to $n = 8.5 \times 10^{12}$ cm^{-2}. For the plain graphene, the gross trends in Fig. 2 repeat the behaviour of gated structures[16,17,25]. At all carrier densities, the dominant fringe (closest to the sample edge) is present, with additional higher-order fringes appearing in the profiles, corresponding to higher carrier densities. For the smallest and largest carrier densities (Fig. 2a,f), both the MPG regions and plain graphene show nearly matching line-profiles. In contrast to plain graphene, in the intermediate doping regime, the line-profiles for MPG areas do not reveal additional, weaker fringes (panels in Fig. 2c–e). Instead, in this regime, MPG samples show an overall increase of the scattering amplitude in the interior of the samples, without additional fringe structure.
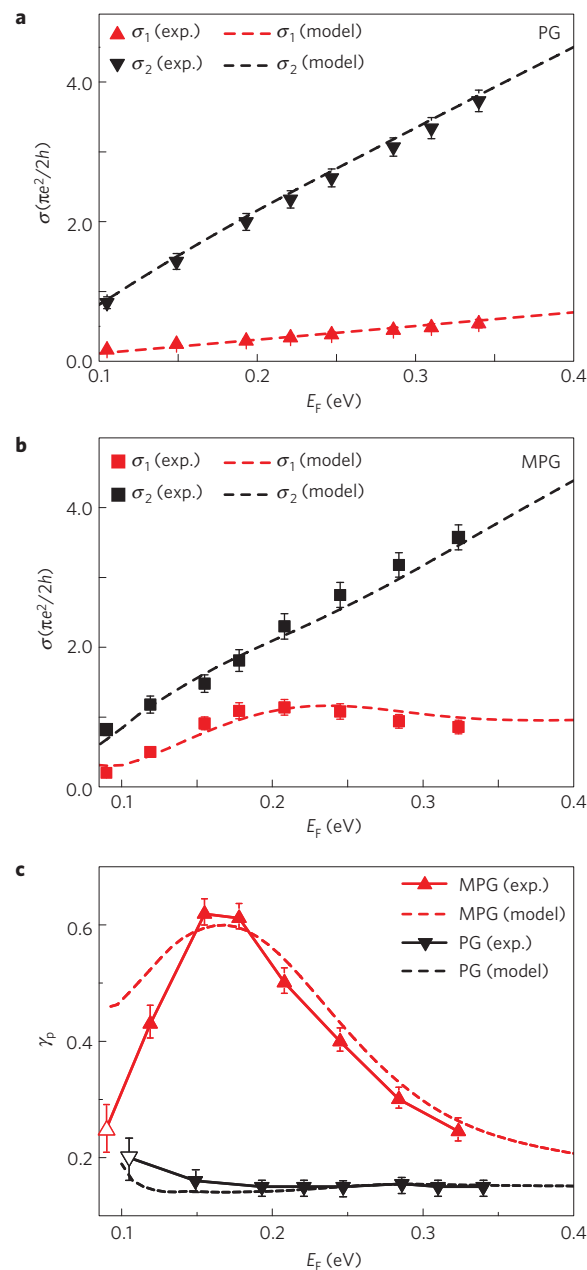
We now proceed to quantitatively analyse the trends seen in MPG and plain graphene. First, we will extract the complex conductivity of graphene from the raw line-profile data (symbols in Fig. 3a,b). Then we will compare these results with the conductivity calculated theoretically for plain and moiré superlattice graphene. The line-profiles in Fig. 2 are uniquely determined by the complex momentum of the plasmon q_p, which, according to equation (1), is directly related to the conductivity of graphene. In Fig. 3a,b we show the conductivity extracted from fitting of plasmonic line-profiles (see Supplementary Information). In the case of plain graphene, the conductivity and the magnitude of E_F are expected to be linearly related according to equation (2). This dependence is obeyed in our plain graphene samples (Fig. 3a). As for the MPG, the connection between the conductivity and the Fermi energy must be evaluated numerically (Supplementary Information). In contrast to the linear change seen in plain graphene, a nonlinear variation of the real part of the conductivity $\sigma_1(\omega = 890$ cm$^{-1})$ with E_F in MPG can be seen in Fig. 3b. Another quantity of interest is the damping factor $\gamma_p \sim \sigma_1/\sigma_2$ (Fig. 3c). In plain graphene the magnitude of γ_p is nearly independent of E_F, whereas in MPG we observe a non-monotonic variation of damping with E_F, with a broad maximum at $E_F \sim 0.2$ eV.

We wish to point out that in addition to the damping caused by the inter-mini-band transitions specific to the superlattice (see below), loss mechanisms present in plain graphene (impurities,
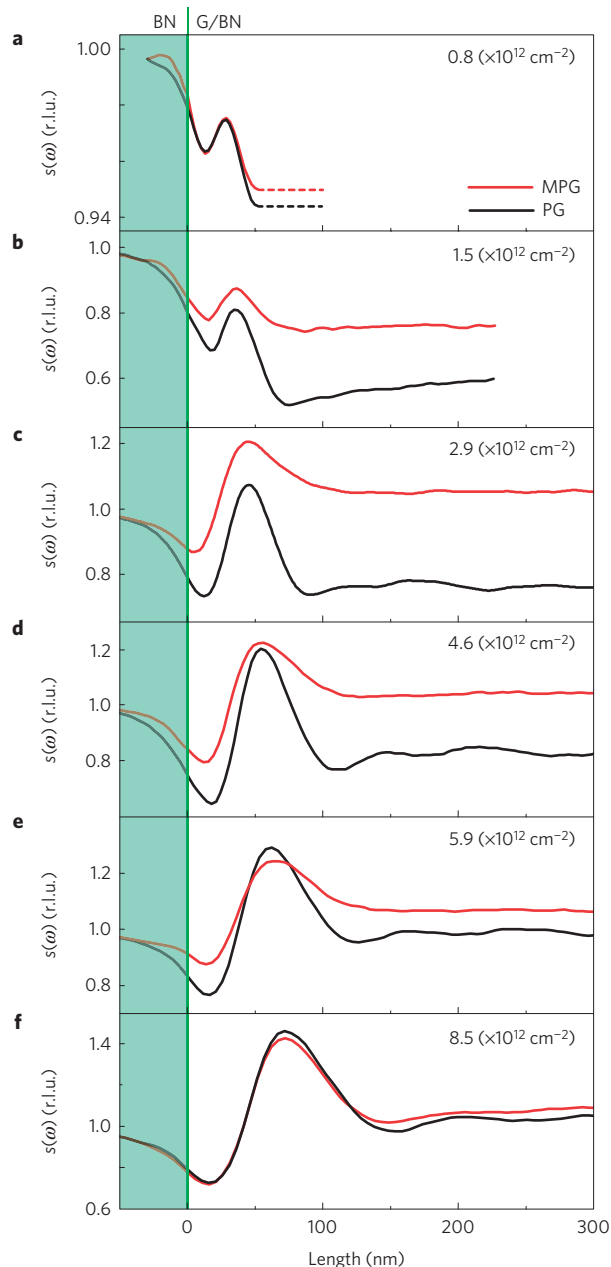
Figure 2 | Plasmonic line-profiles for both moiré-patterned graphene (MPG) and plain graphene (PG) at different carrier densities. These data were collected for specimens with different levels of unintentional doping as marked in the frame. From **a** to **f**, the corresponding plasmon wavelength λ_p increases from 50 nm to 220 nm, as described in the text. The graphene is to the right of the shaded region.

Figure 3 | Extraction of optical conductivity and plasmon damping.
a,b, The red and black data points are the optical conductivity from plain graphene (**a**) and MPG (**b**) extracted from the imaging data at $\omega = 890$ cm^{-1} as a function of Fermi energy E_F. The red and black dashed lines are the modelling results for both σ_1 and σ_2 at room temperature.
c, The red and black data points are the extracted plasmon damping γ_p plotted as a function of E_F from the MPG and plain graphene, respectively. The experimental values of γ_p were obtained from the ratio of σ_1 and σ_2. The open triangles for $E_F \sim 0.1$ eV data points signify a larger uncertainty of fitting at low carrier density. The red and black dashed lines are the modelling results of the plasmon damping rate for both MPG and plain graphene, respectively. The error bars represent the 95% confidence intervals.

electron–electron, electron–phonon interaction) are most certainly present in MPG. Such contributions are likely to be additive, at least, when each of them is weak. Recent calculations of plasmon damping due to electron scattering by impurities[26], other electrons[27] and acoustic phonons[24,25] identified the latter as the dominant dissipation mechanism in high-mobility graphene at ambient. These calculations predict that the relaxation rate, $\tau^{-1}(\omega)$, varies with frequency, which explains why using the transport time from the d.c. conductivity underestimates the plasmon damping at mid-IR frequencies[25]. Our model of plasmon damping, which uses an adjustable and ω-independent parameter τ, is still oversimplified. As moiré graphene is a much more complicated system than plain graphene, a diagrammatic calculation of electron–phonon

scattering[24] is challenging. However imperfect our modelling approach is, it does highlight stark distinctions in the plasmon damping between plain graphene and MPG.

To determine the origin of the measured variation of the complex conductivity of MPG, we consider optical transitions (Fig. 4b,c) enabled by the moiré superlattices, which we computed following
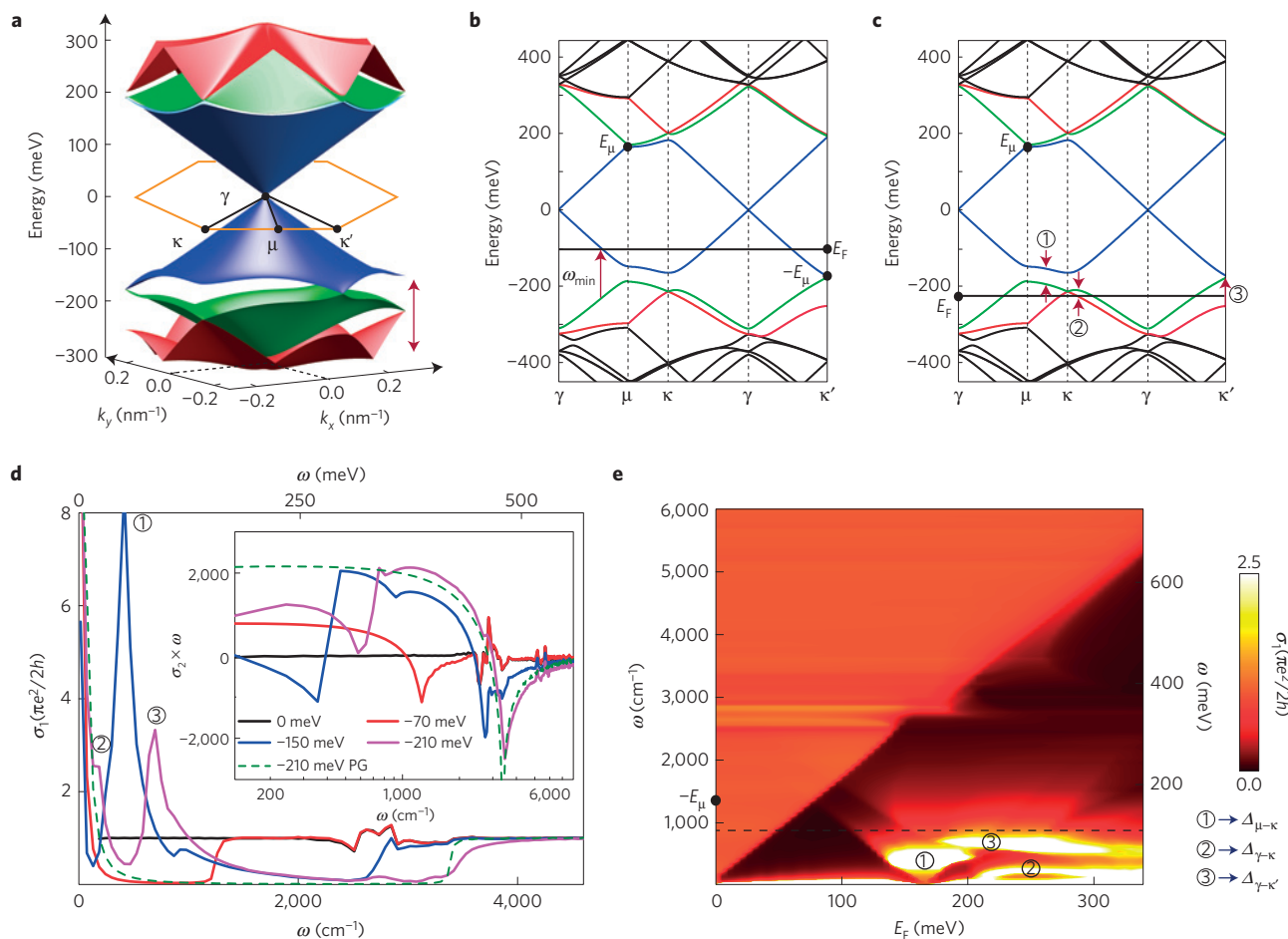
Figure 4 | Electronic band structure and the optical conductivity of graphene moiré superlattices. a, 3D representation of the electronic band structure of MPG obtained from the phenomenological model as described in the Supplementary Information. The impact of the superlattice modulation is more prominent for the hole side than for the electron side. **b,c**, Band structure for MPG presented in the superlattice zone scheme for two different positions of the Fermi level. **b**, For a magnitude of the E_F smaller than E_μ, the moiré potential causes additional optical transitions once the carrier density $n_{min} \sim 6.3 \times 10^{11}$ cm^{-2} is reached. **c**, For a magnitude of E_F larger than E_μ one finds multiple additional channels for optical transitions, all initiated by the moiré potential. These transitions enhance the conductivity and also yield an interband contribution to the plasmonic wavelength in addition to intraband contribution due to the Dirac cones at the γ points. **d**, Theoretical conductivity spectra $\sigma_1(\omega)$ calculated for MPG at different values of E_F in the low-temperature conditions. The dashed green curve represents $\sigma_1(\omega)$ for plain graphene at $E_F = -210$ meV for comparison. Inset shows the product of $\sigma_2(\omega)\omega$ for MPG at different magnitudes of E_F. The dashed green curve represents $\sigma_2(\omega)\omega$ for plain graphene at $E_F = -210$ meV for comparison. **e**, Calculated 2D mapping of σ_1 as a function of ω and E_F. The dashed line indicates the experimental probing frequency of 890 cm^{-1}. The circled numbers 1,2,3 in **c**–**e** represent the superlattice mini-band resonances.

previous studies[3,4,6,15], as detailed in Supplementary Section III. The moiré potential introduces several important energy scales, such as $E_\mu = g\nu_F/2 \approx 170$ meV, where ν_F is the Fermi velocity of plain graphene and $g = 2\pi/\lambda_\mu$ is the superlattice momentum. This energy scale is roughly equal to the electron energy at the μ-points of the mini Brillouin zone (Fig. 4a–c). It defines characteristic features of the particle–hole excitations of MPG that can be recognized in the spectra of the optical conductivity (Fig. 4d,e). Specifically, at $\omega = 2E_\mu$, the $\sigma_1(\omega)$ spectra acquire a weak structure owing to transitions between the μ-points of the conduction and valence bands[6]. Furthermore, in doped (or gated) MPG specimens, the relationship between E_μ and E_F defines characteristic attributes of the optical conductivity in the following three regimes: $|E_F| \ll E_\mu$, $|E_F| \simeq E_\mu$, $|E_F| > E_\mu$ all relevant to the range of carrier densities in the data set shown in Figs 2 and 3.

In weakly doped MPG ($|E_F| \ll E_\mu$), the conductivity is dominated by the low-energy regions of the electron spectra, preserving their Dirac-like character even in the superlattice samples. For simplicity, we assumed here that MPG is incommensurate and has no gap

at the Dirac point[6,10,12]. In this regime, the dominant feature of the conductivity spectra is the onset of transitions between the two linearly dispersing mini-bands (the blue bands in Fig. 4a–c). This step-like onset is seen at $\omega = 1,100$ cm^{-1} in the red trace of Fig. 4d ($E_F = -70$ meV) and as the sharp change near the diagonal of the false colour conductivity map in Fig. 4e, where $\omega = 2E_F$. The interband spectral weight missing below $2E_F$ reappears in the intraband transitions (Drude peak) at $\omega = 0$ (refs 28,29). Apart from the weak features at $2E_\mu$, the conductivities of the plain and weakly doped MPG almost coincide. Accordingly, imaging data in Fig. 2a reveal nearly identical plasmonic patterns.

As doping increases and the magnitude of E_F approaches E_μ, transitions involving another pair of mini-bands (the blue and either the green or the red valence bands in Fig. 4a–c) become significant. The details of the mini-band absorption depend on the assumptions for the potentials describing the interaction of graphene with hBN. One possible outcome is the formation of gapless mini-bands with replicas of Dirac cones. Alternatively, some or all of mini-bands may acquire the energy gaps (Fig. 4b,c): a scenario that most accurately

reproduces the totality of experimental data in Figs 2 and 3, as will be detailed below. Within this latter scenario, the transitions along γ–μ and along γ–κ and γ–κ′ produce threshold features at $\omega_{min} \approx 2E_\mu - 2E_F$ (Fig. 4b) and $\omega \approx [(\sqrt{3}E_\mu - |E_F|)^2 + E_\mu^2]^{1/2} - |E_F|$, respectively. These transitions prompt a pair of the descending diagonal lines in Fig. 4e. Along the μ–κ path, the dispersions of the green and blue valence bands are almost parallel (nested), being separated by $\Delta_{\mu-\kappa} \approx 380\,cm^{-1}$, as indicated in Fig. 4c. Such a nesting is responsible for the strong resonance at $\omega \approx \Delta_{\mu-\kappa}$ in the conductivity spectra when E_F falls within $\sim \Delta_{\mu-\kappa}$ from $-E_\mu$ (the blue trace in Fig. 4d and the leftmost 'hot region' in Fig. 4e). The $\Delta_{\mu-\kappa}$-resonance is directly relevant to the plasmonic imaging data in Fig. 2b–d because its influence remains appreciable at our probing frequency of $890\,cm^{-1}$. This resonance both enhances the overall contrast due to MPG and suppresses weaker (higher-order) plasmonic fringes in these data. At higher E_F two other interband resonances appear (the magenta trace in Fig. 4d and the other two 'hot regions' in Fig. 4e). These are due to the approximate nesting of the green and red valence bands along the γ–κ ($\Delta_{\gamma-\kappa} \approx 200\,cm^{-1}$) and γ–κ′ ($\Delta_{\gamma-\kappa'} \approx 690\,cm^{-1}$) paths in Fig. 4c. (For the chosen simulation parameters the magnitudes of $\Delta_{\mu-\kappa}$, $\Delta_{\gamma-\kappa}$ and $\Delta_{\gamma-\kappa'}$ already deviate by ~20% from the lowest-order perturbative formulae[3].) Overall, the gapped mini-band contribution to $\sigma_1(\omega)$ spectra at the frequency of our plasmonic probe is peaked at the doping level corresponding to $E_F \sim 0.2\,eV$ and is slightly reduced at higher doping. In contrast, gapless mini-bands lead to a monotonic variation of the conductivity with E_F (see Supplementary Information). We therefore conclude that a model of gapped mini-bands is fully consistent with the findings of plasmonic imaging.

To describe the caveats of the measured plasmon wavelength in MPG at appreciable doping levels $|E_F| > E_\mu$, we now turn to the analysis of the product $\sigma_2(\omega)\omega$. These spectra help to illustrate the redistribution of the spectral weight between inter- and intra-mini-band transitions in MPG. In the limit of $\omega \to 0$ this product yields[30] the spectral weight of a narrow Drude peak $\sigma_2(\omega)\omega \approx D$, that in the case of plain graphene is given by equation (2). As expected, in plain graphene the product $\sigma_2(\omega)\omega$ is approximately constant in the range $\tau^{-1} \ll \omega \ll 2E_F$ (Fig. 4d, inset). However, in MPG the low-frequency behaviour of $\sigma_2(\omega)\omega$ is more complicated because of additional inter-mini-band transitions. At $\tau^{-1} \ll \omega \ll \min(\Delta_{\mu-\kappa}, \Delta_{\gamma-\kappa}, \Delta_{\gamma-\kappa'})$, the product $\sigma_2(\omega)\omega$ yields the intra-mini-band part of the spectral weight. As exemplified by the spectrum for $E_F = -210\,meV$, the magnitude of this Drude-like weight is reduced[15] compared to that of the plain graphene of the same Fermi energy, equation (2). As frequency increases, the product $\sigma_2(\omega)\omega$ reveals a minimum in the vicinity of $\omega = 580\,cm^{-1}$, and thereafter plateaus at the same level as in the plain graphene (see the dashed curve in Fig. 4d, inset). The net result is that the magnitude of $\sigma_2(\omega)$ at frequencies far above the inter-mini-band resonances, $\omega \gg \Delta = \max(\Delta_{\mu-\kappa}, \Delta_{\gamma-\kappa}, \Delta_{\gamma-\kappa'})$, is the same in plain graphene and MPG, as demanded by the oscillator strength sum rule[31,32]. Hence, we arrive at the notion of a composite plasmon in moiré superlattices originating from the two additive contributions: the usual Drude channel (that is, of the ungapped portion of the Fermi surface) and the interband channel associated with the superlattice mini-bands (the gapped portion of the Fermi surface). In our data collected at ambient, the differences of response of plain graphene and MPG is masked by finite temperature effects, as $T = 300\,K$ corresponds to approximately $\Delta/3$. We anticipate more prominent near-field contrast and stronger plasmonic reflections at the boundary of plain and moiré graphene at lower T and/or lower frequencies $\omega < \Delta$ (see below and Supplementary Information).

We now wish to outline some implications of our work and some problems for future study. First, we have shown that the interface of plain graphene and MPG acts as a plasmonic reflector with a doping-dependent reflection coefficient (Supplementary

Information). This implies that plasmonic reflectors formed at the boundary between MPG and plain graphene can also be tuned with the single gate voltage applied to the entire structure, which may be advantageous for implementation of graphene plasmonic circuits[33]. These tunable metasurfaces are a prerequisite for the implementation of transformation plasmonics[34], which offers the capability to control plasmonic fields at will and allow novel functionalities that were not previously attainable (Supplementary Information). Second, a more complete experimental picture of the electromagnetic response of the moiré graphene may be obtained by extending our approach to terahertz and far-IR regions where the composite plasmon is predicted to generate an additional low-energy plasmon branch (see ref. 15 and Supplementary Fig. 7). The recent development of alternative broadband light sources, such as synchrotron light or free-electron lasers, opens the door towards nano-imaging experiments at far-IR frequencies[35–40]. Finally, in our model, graphene is assumed to be perfectly rigid and incommensurate with the hBN. It will be worthwhile investigating if plasmonic spectroscopy can reveal subtle topological effects that arise from deformation of the graphene lattice and the induced lattice commensurability[12].

Methods

Methods and any associated references are available in the online version of the paper.

References

1. Dean, C. R. et al. Hofstadter's butterfly and the fractal quantum Hall effect in moiré superlattices. Nature **497**, 598–602 (2013).
2. Xue, J. et al. Scanning tunnelling microscopy and spectroscopy of ultra-flat graphene on hexagonal boron nitride. Nature Mater. **10**, 282–285 (2011).
3. Wallbank, J. R., Patel, A. A., Mucha-Kruczyński, M., Geim, A. K. & Fal'ko, V. I. Generic miniband structure of graphene on a hexagonal substrate. Phys. Rev. B **87**, 245408 (2013).
4. Abergel, D. S. L., Wallbank, J. R., Chen, X., Mucha-Kruczyński, M. & Fal'ko, V. I. Infrared absorption by graphene–hBN heterostructures. New J. Phys. **15**, 123009 (2013).
5. Basov, D. N., Fogler, M. M., Lanzara, A., Wang, F. & Zhang, Y. Colloquium: Graphene spectroscopy. Rev. Mod. Phys. **86**, 959–993 (2014).
6. Shi, Z. et al. Gate-dependent pseudospin mixing in graphene/boron nitride moiré superlattices. Nature Phys. **10**, 743–747 (2014).
7. Yankowitz, M., Xue, J. & LeRoy, B. J. Graphene on hexagonal boron nitride. J. Phys. Condens. Matter **26**, 303201 (2014).
8. Gorbachev, R. V. et al. Detecting topological currents in graphene superlattices. Science **346**, 448–451 (2014).
9. San-Jose, P., Gutiérrez-Rubio, A., Sturla, M. & Guinea, F. Electronic structure of spontaneously strained graphene on hexagonal boron nitride. Phys. Rev. B **90**, 115152 (2014).
10. Chen, Z. G. et al. Observation of an intrinsic bandgap and Landau level renormalization in graphene/boron-nitride heterostructures. Nature Commun. **5**, 4461 (2014).
11. Yu, G. L. et al. Hierarchy of Hofstadter states and replica quantum Hall ferromagnetism in graphene superlattices. Nature Phys. **10**, 525–529 (2014).
12. Woods, C. R. et al. Commensurate–incommensurate transition in graphene on hexagonal boron nitride. Nature Phys. **10**, 451–456 (2014).
13. Hunt, B. et al. Massive Dirac fermions and Hofstadter butterfly in a van der Waals heterostructure. Science **340**, 1427–1430 (2013).
14. Ponomarenko, L. A. et al. Cloning of Dirac fermions in graphene superlattices. Nature **497**, 594–597 (2013).
15. Tomadin, A., Guinea, F. & Polini, M. Generation and morphing of plasmons in graphene superlattices. Phys. Rev. B **90**, 161406(R) (2014).
16. Fei, Z. et al. Gate-tuning of graphene plasmons revealed by infrared nano-imaging. Nature **487**, 82–85 (2012).
17. Chen, J. et al. Optical nano-imaging of gate-tunable graphene plasmons. Nature **487**, 77–81 (2012).
18. Tang, S. et al. Precisely aligned graphene grown on hexagonal boron nitride by catalyst free chemical vapor deposition. Sci. Rep. **3**, 2666 (2013).
19. Tang, S. et al. Silane-catalysed fast growth of large single-crystalline graphene on hexagonal boron nitride. Nature Commun. **6**, 6499 (2015).

20. Yang, W. *et al.* Epitaxial growth of single-domain graphene on hexagonal boron nitride. *Nature Mater.* **12,** 792–797 (2013).

21. Fei, Z. *et al.* Tunneling plasmonics in bilayer graphene. *Nano Lett.* **15,** 4973–4978 (2015).

22. Alonso-González, P. *et al.* Controlling graphene plasmons with resonant metal antennas and spatial conductivity patterns. *Science* **344,** 1369–1373 (2014).

23. Fei, Z. *et al.* Electronic and plasmonic phenomena at graphene grain boundaries. *Nature Nanotech.* **8,** 821–825 (2013).

24. Principi, A. *et al.* Plasmon losses due to electron–phonon scattering: The case of graphene encapsulated in hexagonal boron nitride. *Phys. Rev. B* **90,** 165408 (2014).

25. Woessner, A. *et al.* Highly confined low-loss plasmons in graphene-boron nitride heterostructures. *Nature Mater.* **14,** 421–425 (2015).

26. Principi, A., Vignale, G., Carrega, M. & Polini, M. Intrinsic lifetime of Dirac plasmons in graphene. *Phys. Rev. B* **88,** 195405 (2013).

27. Principi, A., Vignale, G., Carrega, M. & Polini, M. Impact of disorder on Dirac plasmon losses. *Phys. Rev. B* **88,** 121405(R) (2013).

28. Li, Z. Q. *et al.* Dirac charge dynamics in graphene by infrared spectroscopy. *Nature Phys.* **4,** 532–535 (2008).

29. Mak, K. F., Ju, L., Wang, F. & Heinz, T. F. Optical spectroscopy of graphene: From the far infrared to the ultraviolet. *Solid State Commun.* **152,** 1341–1349 (2012).

30. Basov, D. N. *et al.* In-Plane anisotropy of the penetration depth in $YBa_2Cu_3O_{7x}$ and $YBa_2Cu_4O_8$ superconductors. *Phys. Rev. Lett.* **74,** 598–601 (1995).

31. Gusynin, V. P., Sharapov, S. G. & Carbotte, J. P. AC conductivity of graphene: From tight-binding model to 2+1-dimensional quantum electrodynamics. *Int. J. Mod. Phys. B* **21,** 4611–4658 (2007).

32. Sabio, J., Nilsson, J. & Castro Neto, A. H. f-sum rule and unconventional spectral weight transfer in graphene. *Phy. Rev. B* **78,** 075410 (2008).

33. Vakil, A. & Engheta, N. Transformation optics using graphene. *Science* **332,** 1291–1294 (2011).

34. Kadic, M. *et al.* Transformation plasmonics. *Nanophotonics* **1,** 51–64 (2012).

35. Bechtel, H. A., Muller, E. A., Olmon, R. L., Martin, M. C. & Raschke, M. B. Ultrabroadband infrared nanospectroscopic imaging. *Proc. Natl Acad. Sci. USA* **111,** 7191–7196 (2014).

36. Hermann, P. *et al.* Characterization of semiconductor materials using synchrotron radiation-based near-field infrared microscopy and nano-FTIR spectroscopy. *Opt. Express* **22,** 17948–17958 (2014).

37. Fehrenbacher, M. *et al.* Plasmonic superlensing in doped GaAs. *Nano Lett.* **15,** 1057–1061 (2015).

38. Hegenbarth, R. *et al.* High-power femtosecond mid-IR sources for s-SNOM applications. *J. Opt.* **16,** 094003 (2014).

39. Bensmann, S. *et al.* Near-field imaging and spectroscopy of locally strained GaN using an IR broadband laser. *Opt. Express* **22,** 22369–22381 (2014).

40. Huber, A. J., Keilmann, F., Wittborn, J., Aizpurua, J. & Hillenbrand, R. Terahertz near-field nanoscopy of mobile carriers in single semiconductor nanodevices. *Nano Lett.* **8,** 3766–3770 (2008).

Author contributions

All authors were involved in designing the research, performing the research, and writing the paper.

Additional information

Supplementary information is available in the online version of the paper. Reprints and permissions information is available online at www.nature.com/reprints. Correspondence and requests for materials should be addressed to D.N.B.

Competing financial interests

F.K. is one of the co-founders of Neaspec, producer of the s-SNOM apparatus used in this study.

Methods

Hexagonal boron nitride (hBN) flakes were prepared on quartz substrates using mechanical exfoliation. Graphene microcrystals were then epitaxially grown on top of hBN using a catalysis-free chemical vapour deposition (CVD; ref. 18). First, the hBN flakes on quartz were annealed at 1,150 °C at low pressure with a continuous argon flow of 50 standard cubic centimetres per minute (sccm) for 30 min. Then, graphene was grown on the hBN flakes at 1,150 °C by flowing CH_4:H_2 at 5:5 sccm for 300 min at pressures below 12 mbar. After growth, samples were cooled to room temperature in argon flow. The morphology, grain size, shape and crystallographic orientation of the CVD graphene can be controlled by varying growth conditions. Clusters of polycrystalline graphene are often detected in samples grown at a lower temperature. In macroscopic samples prepared using catalyst-free synthesis, MPG ($\lambda_\mu \sim 14$ nm, $\theta \sim 0°$) regions commonly reside next to plain graphene ($\lambda_\mu < 0.5$ nm, $\theta \sim 30°$): a virtue that

allowed us to examine the impact of the moiré superlattice in the same particular microcrystals.

The infrared nano-imaging experiments were performed using a scattering-type scanning near-field optical microscope (s-SNOM). Our s-SNOM (http://www.neaspec.com) is equipped with continuous-wave mid-IR quantum cascade lasers (http://www.daylightsolutions.com) and CO_2 lasers (http://www.accesslaser.com). The s-SNOM is based on an atomic force microscope (AFM) operating in the tapping mode with a tapping frequency around 270 kHz. A pseudo-heterodyne interferometric detection module is implemented in our s-SNOM to extract both the scattering amplitude s and phase ψ of the near-field signal. In the current work, we discuss the amplitude of the signal. To subtract the background signal, we demodulated the near-field signal at the third harmonic of the tapping frequency. All the infrared nano-imaging experiments were performed in ambient conditions.

Plasmons in graphene moiré superlattices

G. X. Ni[1,2], H. Wang[3], J. S. Wu[2], Z. Fei[2], M. D. Goldflam[2], F. Keilmann[4], B. Özyilmaz[1], A. H. Castro Neto[1], X. M. Xie[3], M. M. Fogler[2], D. N. Basov[2*]

[1]Centre for Advanced 2D Materials and Graphene Research Centre, National University of Singapore, Singapore, 117546.

[2]Department of Physics, University of California, San Diego, La Jolla, California 92093, USA.

[3]State Key Laboratory of Functional Materials for Informatics, Shanghai Institute of Microsystem and Information Technology, Chinese Academy of Sciences, 865 Changning Road, Shanghai 200050, P. R. China.

[4]Ludwig-Maximilians-Universität and Center for Nanoscience, 80539 München, Germany.

[*]Corresponding author email address: dbasov@physics.ucsd.edu

CONTENTS

1. **Raman spectroscopy**
2. **Plasmon line-profile fitting**
3. **Electronic band structure and optical conductivity of moiré patterned graphene**
4. **Theoretical results for plasmon dispersions in moiré patterned graphene**
5. **Frequency dependent study of plasmonic signal s(ω) in plain and moiré patterned graphene**
6. **Tunable plasmonic reflector at the boundary between moiré patterned and plain graphene**

1. Raman spectroscopy

In Fig. S1, we plot Raman spectra for both moiré patterned graphene (MPG) and plain graphene (PG). For the PG, the full width at half maximum (FWHM) is ~ 21 cm^{-1}, attesting to the high quality of our single layer specimens. In contrast, the FWHM of MPG is as wide as 43

cm^{-1}. These results are consistent with previous Raman studies of moiré patterned graphene, where considerable broadening of the 2D peak was reported[1].
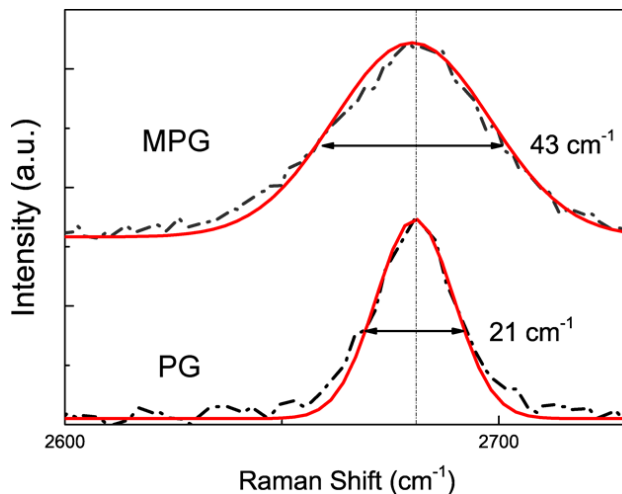
Figure S1 | Raman spectroscopy characterization. The Raman spectra of both MPG and plain graphene graphene at the 2D peak position. Red lines are fits using Lorentzian functions.

2. Plasmon line-profile fitting

We employed the spheroidal tip model of the near-field response[2] to simulate the s-SNOM signal. This approach gives a reasonable compromise between accuracy and the computational cost. The parameters of model include the plasmon wavelength and the plasmon damping ($\gamma_p \sim \sigma_1/\sigma_2$). Representative results are plotted in Fig. S2 and the input parameters are summarized in Table 1. The hBN substrate is modeled as a medium with the effective permittivity $\varepsilon_{sub}(890 \text{ cm}^{-1}) = 4.56$, the geometric mean of the in-plane and out-of-plane permittivities of hBN[3-5]. Here the utilization of geometric mean as the effective permittivity of hBN is justified as the hBN slab can be approximated by an infinite half-space when the condition of $d > \lambda_p/2\pi$ was satisfied. We also report the carrier density in Table 1 (The carrier densities were calculated using Eq. 3 in the main text).
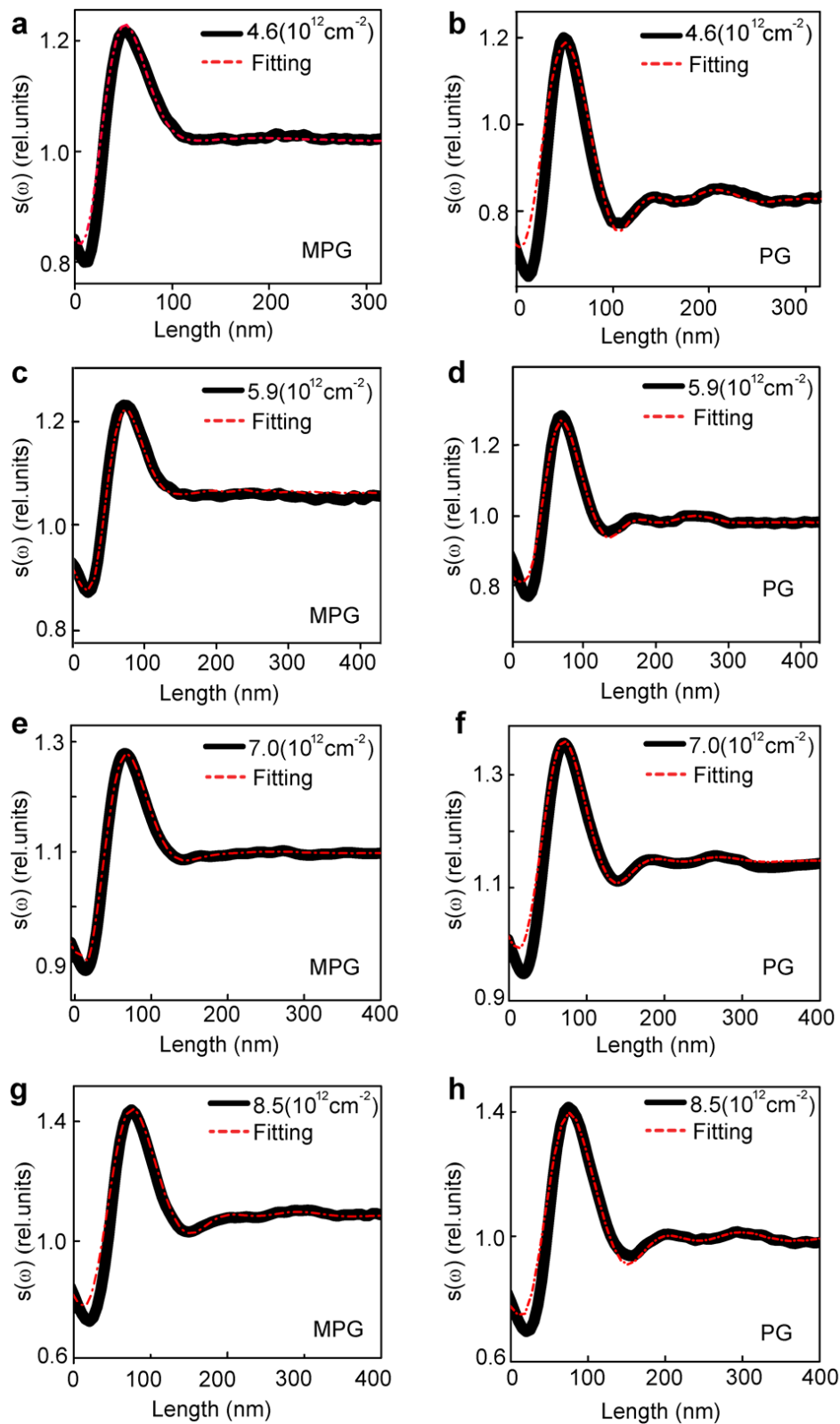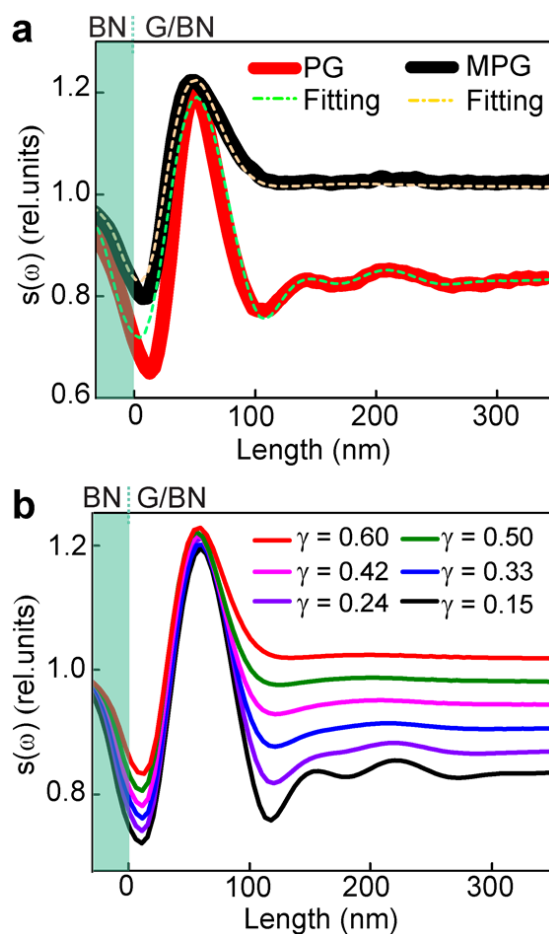
Figure S2 | Plasmon line-profile fitting. Panels a, c, e, g: plasmon line-profiles for MPG specimens with various carrier densities. Panels b, d, f, h: plasmon line-profiles for PG. Panels in the same raw present data for PG and MPG regions of the same graphene microcrystal with the plasmonic response governed by the same carrier densities. The black solid lines are the experimental data; the red dashed lines are the theoretical fits using the spheroid model. Fitting parameters are presented in Table 1.

Samples Parameter	Fig.S2a MPG	Fig.S2b PG	Fig.S2c MPG	Fig.S2d PG	Fig.S2e MPG	Fig.S2f PG	Fig.S2g MPG	Fig.S2h PG
Plasmon wavelength (nm)	165	157	180	178	199	193	217	219
Plasmon damping (γ_p)	0.55	0.155	0.5	0.155	0.35	0.155	0.22	0.165
Carrier density (10^{12} cm^{-2})	4.6	4.6	5.9	5.9	7.0	7.0	8.5	8.5

Table 1 | Plasmon line-profile fitting parameters for both MPG and plain graphene (PG) at different carrier densities. The AFM tip radius and tapping amplitude were kept constant at s ~ 25 nm to match the experimental conditions.

The parameters governing plasmon losses and damping in our structures can be determined by examining the decaying plasmon fringe profiles. Fig. S3 present the spheroid model fitting results for one specific plasmonic line profile at different values of the plasmon damping rate γ_p. Here the γ_p varies from ~ 0.15 all the way to ~ 0.60 (Fig. S3b). At low damping rate ($\gamma_p = 0.15$), additional higher order fringes can be clearly seen. However, these higher order fringes are gradually suppressed and eventually disappear with the increase of the plasmon damping rate. When γ_p reaches 0.60, only the most prominent plasmon peak near the sample edge can be recognized.

Figure S3: **Plasmon line-profiles and plasmon damping. a**, Experimental line profiles across graphene edge for both moiré patterned graphene (MPG, solid black) and plain graphene (PG, solid red) reproduced from Fig. S2a&b. The corresponding fitting parameters are summarized in Table 1. The dotted green ($\gamma_p = 0.15$) and orange ($\gamma_p = 0.60$) traces are the calculated line-profiles for two different damping rates using the spheroid model described above. Graphene is on the right side of the shaded region. **b**, Model line-profiles calculated for different choices of the plasmon damping rate γ_p, from 0.15 to 0.60.

3. Electronic band structure and optical conductivity of moiré patterned graphene

The phenomenological model for graphene on the hBN substrate is described by the Hamiltonian[6]

$$H = v\mathbf{p}\boldsymbol{\sigma} + V(\mathbf{r})\xi\mathbf{A}(\mathbf{r})\boldsymbol{\sigma} + \xi\Delta(\mathbf{r})\sigma_z , \qquad (S1)$$

where $\xi = \pm1$ corresponds to valleys K and K', respectively. The spinor wavefunctions

$(\psi_A, \psi_B)^T$ of this 2×2 matrix Hamiltonian represent quantum amplitudes of the Bloch functions on A and B graphene sublattices. The scalar potential $V(\mathbf{r})$, vector potential $\mathbf{A}(\mathbf{r})$, and the mass term $\Delta(\mathbf{r})$ are given by:

$$V(\mathbf{r}) = 2V_s \sum_{m=1}^{3} \cos \mathbf{g}_m \mathbf{r}, \tag{S2}$$

$$\Delta(\mathbf{r}) = -2V_\Delta \sum_{m=1}^{3} (-1)^{m+1} \sin \boldsymbol{g}_m \mathbf{r}, \tag{S3}$$

$$\mathbf{A}(\mathbf{r}) = -2V_A \sum_{m=1}^{3} (-1)^{m+1} [\hat{\mathbf{z}} \times \hat{\mathbf{g}}_m] \cos \boldsymbol{g}_m \boldsymbol{r}, \tag{S4}$$

where $\mathbf{g}_m$'s are the moiré lattice vectors, each of length $|\mathbf{g}_m| \equiv g = 2\pi/\lambda_\mu$ (Fig. S4). The values of the coupling constants (V_s, V_Δ, V_A) are model-dependent[7] and considered as adjustable parameters. In the main text, we chose to restrict ourselves to one adjustable parameter V_0 and to define the coupling constants by

$$(V_s, V_\Delta, V_A) = \left(\frac{1}{2}, -1, -\frac{\sqrt{3}}{2}\right) V_0 . \tag{S5}$$

As presented in Fig. 4, this choice (also used previously in ref. 8) leads to a reasonably good agreement between the measured and the calculated optical conductivity using $V_0 = 14$ meV. Without trying to explore the entire three-parameter phase space, which will be impractical, we point out that another representative choice of moiré parameters $\left(\frac{1}{2}, 0, 0\right) V_0$ (Fig. S5) gives poor agreement with the data.
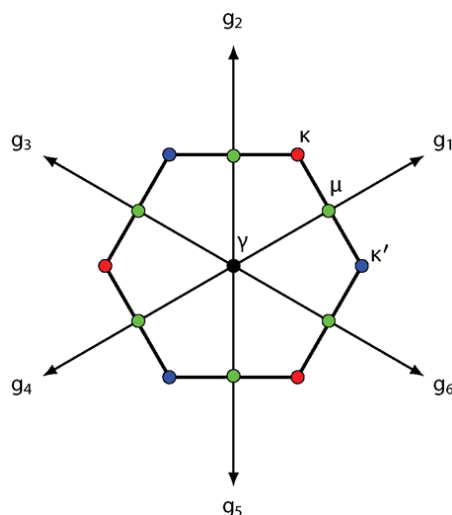
Figure S4 Superlattice Brillouin zone for graphene-hBN moiré structures.

The first step in the conductivity calculation is to obtain the eigenfunctions and eigenvalues of the Hamiltonian (Eq. S1). To this end we project the Hamiltonian onto a reduced basis of plane waves $\exp[i(\mathbf{k} + \mathbf{G})\mathbf{r}] \otimes |\sigma_z\rangle$. Here $\mathbf{k}$ is the wave vector within the superlattice Brillouin zone (SBZ), $\mathbf{G}$ denotes arbitrary linear combinations of $\mathbf{g}_m$, and $|\sigma_z\rangle$ denotes the eigenspinor of σ_z. We restrict the plane wave basis to $|\mathbf{G}| \leq 2g$, which gives the total of 38, $1 \leq m \leq 38$ states and diagonalized the corresponding 76×76 matrix numerically. The calculated energy minibands are shown in Fig. 4a-c of the main text.

The next step is to evaluate the conductivity from the Kubo formula

$$\sigma(\omega) = \frac{g_s g_v i\hbar}{4\pi^2} \int d^2\mathbf{k} \sum_{n,m} \frac{f(E_n) - f(E_m)}{E_m(\mathbf{k}) - E_n(\mathbf{k})} \frac{e^2 v^2 |\langle n|\sigma_x|m\rangle|^2}{\hbar\omega + i\Gamma - E_m(\mathbf{k}) + E_n(\mathbf{k})} , \qquad \text{(S6)}$$

where the integral is taken over the SBZ and $f(E) = \{1 + e^{(E-E_F)/T}\}^{-1}$ is the Fermi-Dirac distribution function. For $m = n$ terms in the sum, describing the intra-band contributions, the first fraction should be replaced by $-f'(E_m)$. We computed the optical conductivity from Eq. S6 by the numerical quadrature utilizing the usual Monkhorst-Pack grid over the SBZ. The broadening Γ in Eq. S1 was determined by fitting the γ_p *vs.* E_F data shown in Fig. 3 of the main text. For plain graphene, this dependence is rather flat. We used $T = 300$ K in the numerical calculations.

Figure S5a show the calculated gapless minibands band structures by turning off graphene-hBN coupling constants V_Δ and V_A in Eq. S5. From its corresponding conductivities results (Fig. S5b), it clearly shows that the corresponding band structure of nearly gapless minibands leads to a monotonic variation of the conductivities *vs.* E_F, which is distinctly different from the observed non-linear conductivity variations (Fig. 3). Thus, we rule out the gapless minibands possibility and conclude that our findings of plasmonic images are consistent with the gapped minibands model.
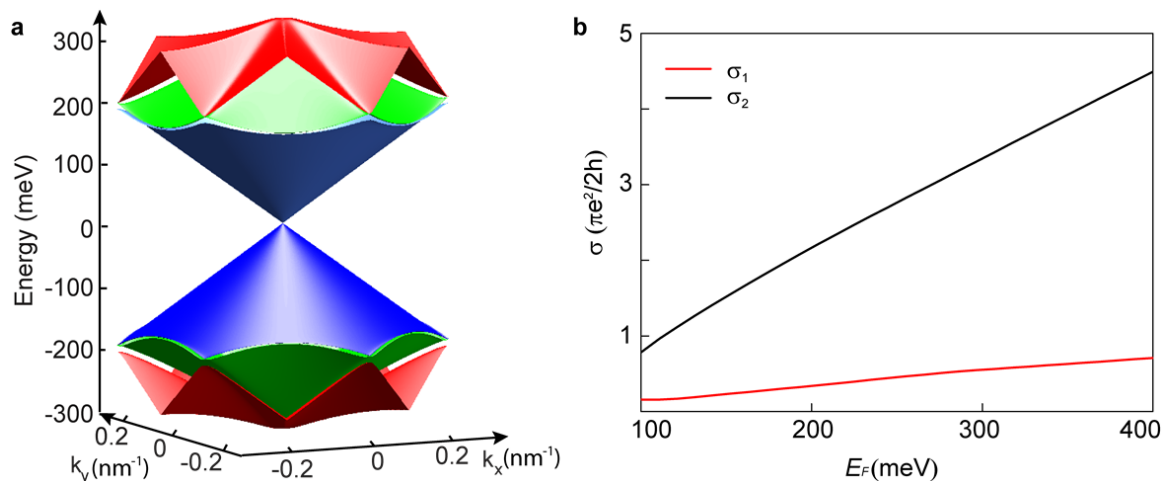
Figure S5 Calculated bands structure and conductivities of graphene moiré superlattices in the case of nearly gapless minibands possibility. a, 3D representation of the electronic band structure of moiré patterned graphene obtained from the phenomenological model as described above. Here the coupling constants $(V_s, V_\Delta, V_A) = \left(\frac{1}{2}, 0, 0\right)V_0$. **b,** Theoretical modeling results for both σ_1 and σ_2 at room temperature.

4. Theoretical results for plasmon dispersions of moiré patterned graphene

Having computed the optical conductivity (Sec. 3), we calculate the plasmon dispersion of MPG using Eq. 1 of the main text with and without considering plasmon-phonon coupling effect. The results are illustrated in Fig. S6. As one can see, at low doping (the $E_F = -50$ meV trace), the dispersion is close to that in plain graphene. The plasmon momentum is quadratic in frequency, in agreement with Eq. 3 of the main text. As doping increases and the Fermi energy approaches the miniband region of the electronic structure, several new distinct features not present in plain graphene develop at low frequencies. In a recent theoretical work[9] these features were dubbed "morphing" and "splitting" of graphene plasmons. Namely, as E_F approaches E_μ (the $E_F = -150$ meV trace in Fig. S6), the low-frequency part of the plasmon frequency becomes much flatter than that in the plain graphene. As discussed in the main text, this is a consequence of the reduction in the $\omega = 0$ Drude weight. The physical reason for this reduction is the breaking of the Fermi surface into small pockets surrounding at the κ and κ' points of the SBZ. Next, there is a range of intermediate frequencies centered around $\omega \sim \Delta = 380\,\mathrm{cm}^{-1}$, i.e., the

region of the strong miniband resonances discussed in the main text. At such ω the plasmons are overdamped, $\Im q_p(\omega) > \Re q_p(\omega)$. These parts of the dispersion curves are unphysical and are excluded in Fig. S6. At even higher frequencies, $\omega > \Delta$, the underdamped, well-defined plasmon re-emerges. At such ω, both the gapless parts of the Fermi surface (the κ and κ' pockets) and the gapped parts (the inter-miniband transitions) act together to create 'composite' plasmons. These plasmons carry the Drude weight of magnitude close to that in the plain graphene. As the doping is increased further (the E_F = -250 meV trace in Fig. S6), both the low and the high frequency branches stiffen, so that the interval of overdamped plasmons moves to lower momenta.
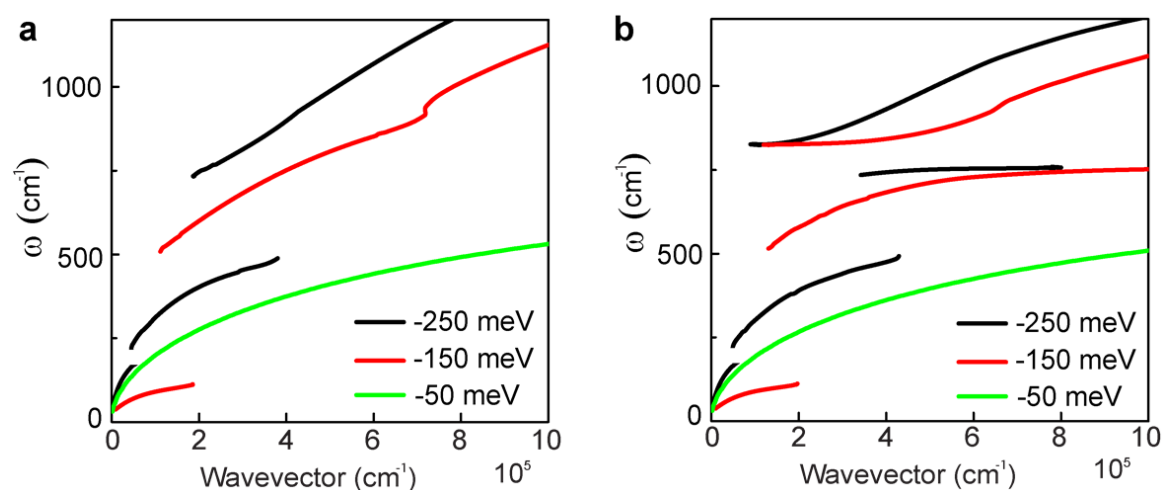
Figure S6 Calculated plasmon dispersions for moiré patterned graphene at different Fermi energies. a, Hypothetical plasmon dispersion calculated using constant substrate permittivity ε_{sub} = 4.56, which amounts to neglecting plasmon-phonon coupling. At low doping, E_F = -50 meV, the plasmon dispersion is the same as plain graphene. However, as E_F approaches E_μ (the E_F = -150 and -250 meV traces), plasmon dispersion splits into two branches separated by an interval where the plasmons are overdamped (see text). **b**, Once the plasmon-phonon coupling is included by using the frequency-dependent ε_{sub}, further splitting of the surface plasmon modes arises near the hBN c-axis phonon resonances.

Another insight into the behavior of the plasmon dispersion in MPG can be obtained considering how the plasmon wavelength λ_p varies as a function of E_F at a constant probing frequency that is used to investigate plasmons in nano-IR experiments. From the above discussion of Fig. S6, one can anticipate to find different results at the probing frequencies that

are higher and lower than the miniband resonance region, $\omega \sim \Delta$. We begin with the results computed for our probing frequency of $890 \, \text{cm}^{-1}$, which is above Δ. The corresponding dispersion curves are shown in Fig. S7a. The solid red curve, computed for the temperature $T = 300 \, \text{K}$ of the experiment, is the basis for determining E_F from the measured λ_p. Unlike plain graphene (the black curve in Fig. S7a), the relation between λ_p and E_F is nonlinear. Specifically, a given plasmon wavelength is generally reached at smaller E_F in MPG than in plain graphene. The largest relative difference is about 20 % at $\lambda_p \sim 150 \, \text{nm}$ where $E_F \sim E_\mu = 0.17 \, \text{eV}$: the regime where the Fermi surface consists of small pockets, as described above. The dashed blue curve in Fig. S7a is our theoretical prediction at $T = 30 \, \text{K}$ for comparison. As one can see, at this T the E_F *vs*. λ_p curve consists of several disconnected branches separated by small gaps inside which the plasmons are overdamped. In Fig. S7b we plot theoretical results for the plasmon dispersion computed for frequency $\omega = 290 \, \text{cm}^{-1}$, which is below the miniband resonance Δ. Looking at the red solid line (for $T = 300 \, \text{K}$) we see, first of all, that at certain range of E_F near E_μ, the plasmons are absent being overdamped by the miniband resonances. Plasmon wavelength above and below this range of Fermi energies differs by almost a factor of two. As discussed above, this difference is due to different spectral weight carried by the low- and the high-frequency plasmon branches: the former comes from the gapless Fermi pockets; the latter also includes the spectral weight from the inter-miniband resonances. Another qualitative change between Fig. S7a and Fig. S7b is that at $\omega = 290 \, \text{cm}^{-1} < \Delta$ the Fermi energy is *larger* in MPG than in plain graphene for the same plasmon wavelength λ_p. The dashed blue curve in Fig. S7b (for $T = 30 \, \text{K}$) displays the same qualitative features as the red solid line, except the upper dispersion branch is broken into several pieces, similar to Fig. S7a, and the lower dispersion branch is much more pronounced. Clearly, both room-temperature and cryogenic s-SNOM experiments, once these are possible, will be of interest at this frequency.
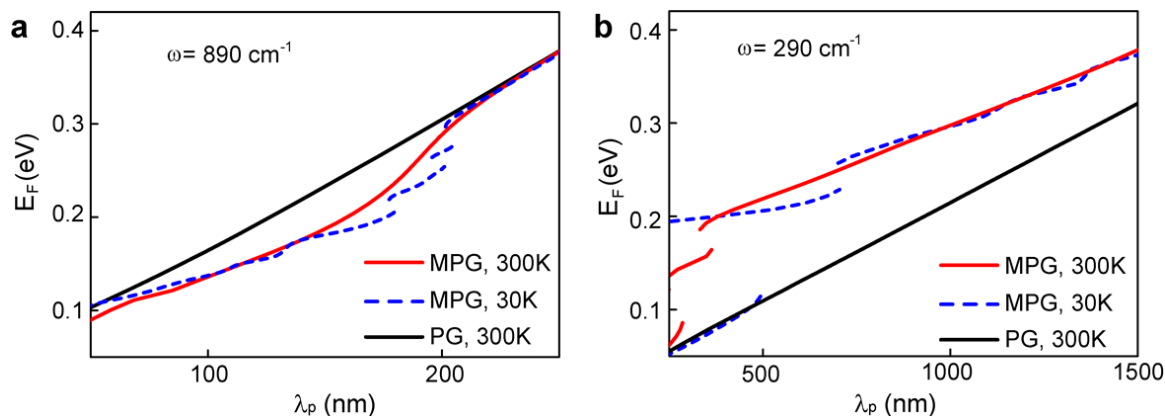
Figure S7. Calculated Fermi energy E_F as a function of plasmon wavelengths for both moiré patterned and plain graphene at two different frequencies. a, E_F *vs.* λ_p computed at ω=890 cm^{-1}, our probing frequency. The red solid (blue dashed) line is for MPG at $T = 300$ K ($T = 30$ K). The black line is for PG at 300 K; **b**, Same as panel A for the probing frequency $\omega = 290$ cm^{-1}. The part of the dispersion where the plasmons are overdamped in a and b is removed (red solid and blue dashed line). The sharp change in λ_p across the damped region is due to the composite plasmon nature at higher Fermi energies.

5. Frequency dependent study of plasmonic signal s(ω) in plain and moiré patterned graphene

Distinct plasmonic response observed in MPG and plain graphene at the probing frequency ω of 890 cm^{-1} is discussed in the main text. Additional nano-imaging data are presented in Fig. S8a&b where we display data for the same sample obtained at probing frequencies 890 cm^{-1} and 1550 cm^{-1}. At the probing frequency ω = 1550 cm^{-1}, we find little difference between the MPG and plane graphene (Fig. S8b). Moreover, for both MPG and plain graphene multiple fringes were detected near the graphene edge, as shown in Fig. S8c. We have also carried out spectroscopic studies of our samples using a broadband laser based light source (Fig. S8d). This broadband source is based on difference frequency generation (DFG) of two femtosecond pulses. Even though the average power of the DFG source is low, the intensity of the electric field is quite high and exceeds 100 kV/cm[10]. These intense fields inevitably lead to electronic heating of graphene, causing additional damping and possibly introducing additional Drude weight. Therefore, a direct comparison between broadband and CW measurements is difficult. However, the problems outlined above may be alleviated in synchrotron-based nano-IR studies[11-13]. In order to further elucidate this frequency dependence, we calculated the optical

conductivity spectra over a wide frequency range, as shown in Fig. S8e. Here we choose the E_F = -210 meV as an example. Clearly, the optical conductivity difference between MPG and plain graphene at ω = 890 cm^{-1} is much larger compared to the data at to 1550 cm^{-1}. This frequency dependent optical conductivity variation generally accounts for the observed frequency dependent plasmon scattering amplitude s(ω) in MPG and plain graphene.
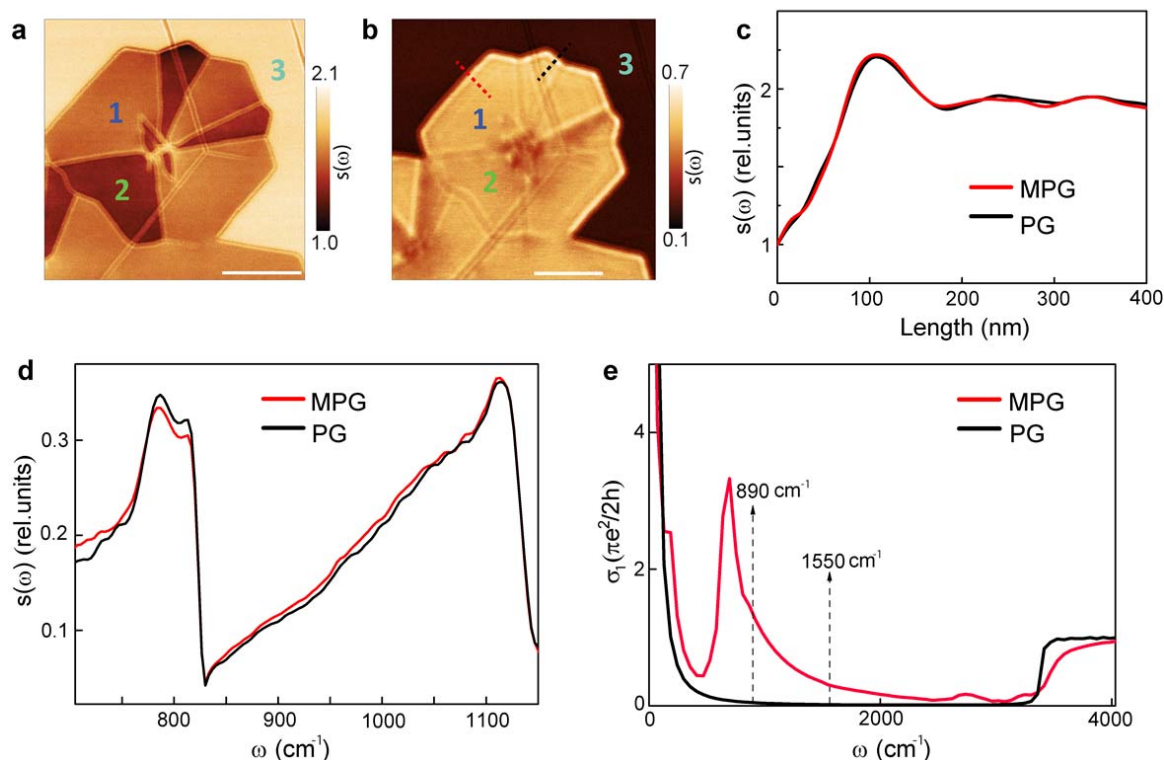
Figure S8 s(ω) nanoimaging and optical conductivities for MPG and plain graphene. a&b, nanoimaging results of a graphene microcrystal containing both MPG and plain graphene carried out at frequencies of 890 and 1550 cm^{-1}. Region "1" corresponds to the moiré patterned graphene, while the region "2" corresponds to non-patterned plain graphene. Region "3": bare hBN. At ω=1550 cm^{-1}, we find little difference between the nano-IR signal for MPG and plane graphene. The scale bar in A and B is 1 μm. **c**, Plasmonic line profiles for both MPG regime (red) and PG regime (black) at ω=1550 cm^{-1}.Higher order fringes interior to the graphene edge were observed in both MPG and PG regime. **d**, Broadband plasmon spectra of both MPG and plain graphene over the frequency range of 700 cm^{-1} to 1150 cm^{-1}. The most prominent aspect of the spectra is present of two strong peaks. The first peak at ~ 780 cm^{-1} is attributed to the c-axis phonon resonance of hBN, while the second peak at around ~1120 cm^{-1} is attributed to the phonons of the underlying quartz substrate. One can also notice that the s(ω) signal for MPG is slightly larger than that of plain graphene (~ 900 cm^{-1}), which is consistent with our nano-imaging results.

e, Theoretically calculated real conductivity spectra for moiré patterned graphene at $T = 3$K. The optical conductivity at 890 cm^{-1} is much larger than the case of 1550 cm^{-1}. This is consistent with the experimental observation in panels a and b.

6. Tunable plasmonic reflector at the boundary between moiré patterned and plain graphene

As described in the main text, the adjacent MPG and plain graphene regions with different conductivities facilitate the realization of self-assembled plasmonic reflectors. Plasmonic reflectors are an essential element of plasmonic circuits and two-dimensional optical components. In our opinion, these elements bring us closer to the implementation of transformational plasmonics: the notion of controlling propagating plasmons by modifying the properties of the media supporting the plasmons[14]. The advantage of these tunable reflectors is that they only require one single gate to control the reflection coefficient of plasmons. Fig. S9 shows a systematic variation of the plasmon fringes across the MPG and plain graphene boundary for samples with different carrier densities. The plasmon reflection coefficient r_{sp} at the plain-MPG boundary can be crudely estimated by modeling it as a step-like discontinuity of the plasmon momentum. We neglect any effects due to elastic strain, lattice misorientation, point defects, or extra damping at the boundary.[15-18] Provided the magnitude of $\Delta q_p = q_{p,\mathrm{MPG}} - q_p$ of the step discontinuity is a small fraction of q_p ($q_{p,\mathrm{MPG}}$ and q_p are the plasmon momentum for both MPG and plain graphene, respectively), the perturbation theory outlined in our previous work (see Supplementary information of ref. 15) applies. It yields the reflection coefficient

$$r_{sp} \simeq i \int_0^\infty \left(q_p - q_{p,\mathrm{MPG}} \right) e^{2iq_p x} dx = i \frac{q_p - q_{p,\mathrm{MPG}}}{-2iq_p} \simeq \frac{q_{p,\mathrm{MPG}} - q_p}{q_{p,\mathrm{MPG}} + q_p}. \qquad \text{(S7)}$$

The convergence of the integral is ensured by the fact that q_p always has some positive imaginary part. The last equation of (S7) possesses the symmetry expected of the exact reflection coefficient and so it is the preferred form. Using $q_{p,\mathrm{MPG}}$ and q_p computed from the optical conductivities by means of Eq. 1 of the main text, r_{sp} can be readily obtained.

Figure S10 shows thus estimated reflectance $|r_{sp}|^2$ as a function of the carrier density. The maximum $|r_{sp}|^2$ of more than 5% was obtained at the carrier density of $\sim 2.9 \times 10^{12}$ cm^{-2},

which corresponds to the Fermi energy E_F of ~0.2 eV. Recall that the moiré superlattice energy $E_\mu = gv_F/2 \approx 170$ meV, this indicates that the maximum reflection coefficient is closely correlated with the electronic band structure. When the E_F is far away E_μ, the reflection coefficient between MPG and PG is low; however, as the E_F approaches to the miniband regime, maximum reflection coefficient is expected. Moreover, it is also expected that the reflection coefficient is frequency dependent. Much stronger reflectance is anticipated at frequencies $\omega < \Delta$ where the difference between the plasmon wavelength in MPG and plain graphene is significantly higher according to the calculation reported in Fig. 4e of the main text. Finally, we wish to comment on the relationship between the reflection coefficient and the plasmon dissipation rate. Currently, the plasmon damping rate in plain graphene is $\gamma_p \sim 0.15$, which could be substantially reduced by further device optimization, for example, by encapsulating graphene in hBN using another hBN layer on top. Reduced plasmon dissipation in plain graphene should lead to an enhanced plasmon reflection coefficient at the plain-MPG boundary.
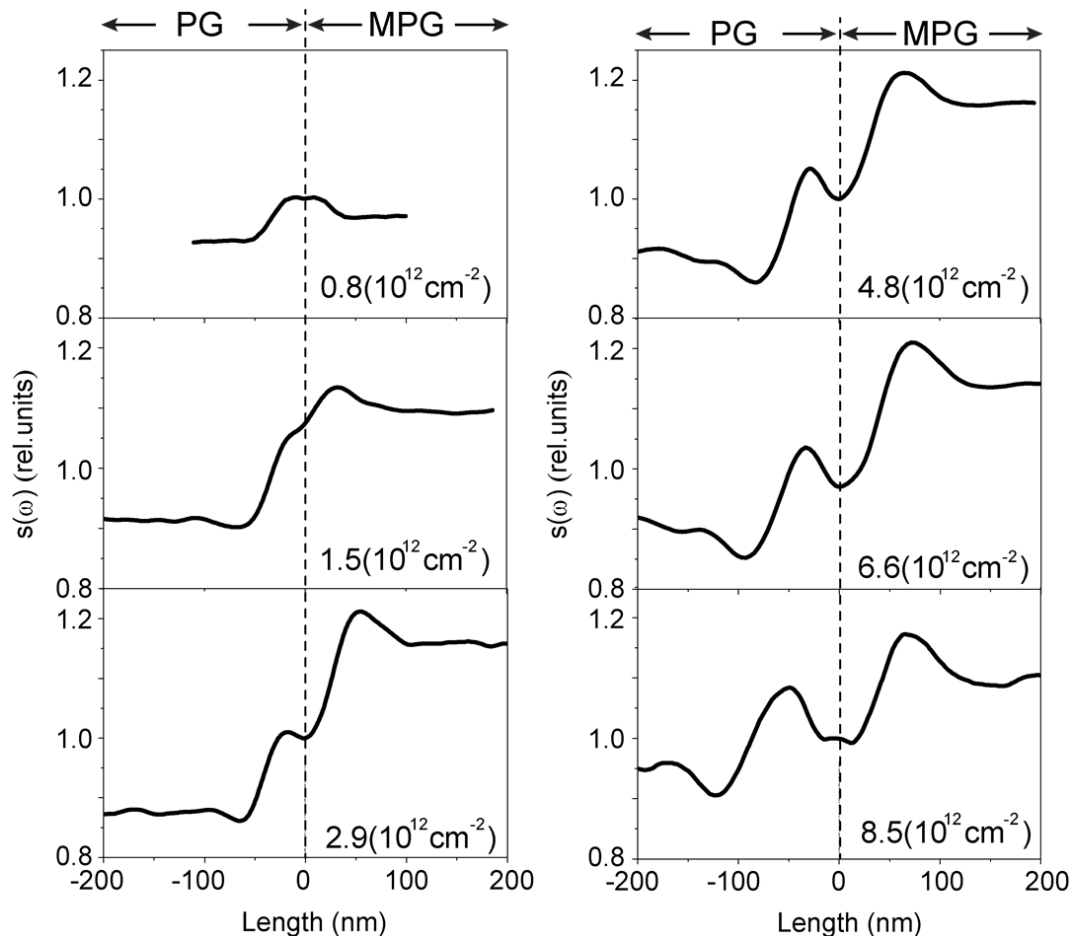
Figure S9 | Plasmonic interference profiles taken across the boundaries of PG and MPG at different carrier densities. These line-profiles were obtained at the frequency of 890 cm^{-1}.
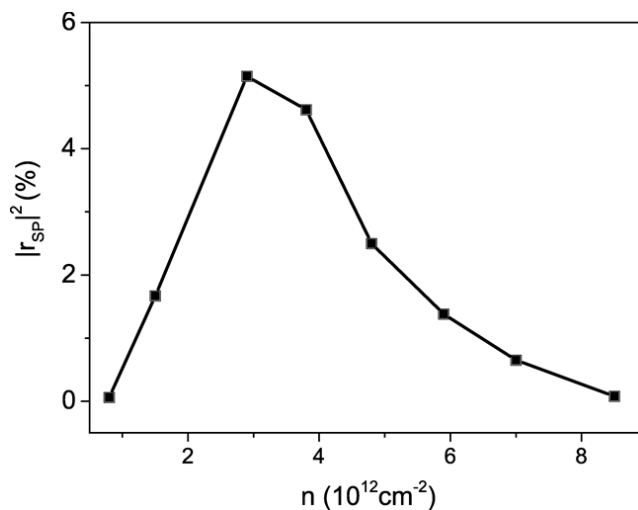
Figure S10 | Calculated plasmonic reflectance at the boundaries between MPG and PG at the frequency of 890 cm⁻¹.

References

1. Eckmann, A. et al. *Nano Lett*. **13**, 5242 (2013).

2. Fei, Z. *et al. Nature* **487**, 82-85 (2012).

3. Principi, A. *et al., Phys. Rev. B* **90**, 165408 (2014).
4. Caldwell, J. D. *et al. Nature. Commun*. **5**, 5221 (2014).

5. Dai, S. Y. *et al. Science* **343**, 1125 (2014).
6. Abergel, D. S. L., Wallbank, J. R., Chen, X., Mucha-Kruczyński, M., Fal'ko, V. I. *New J. Phys*. **15**, 123009 (2013).
7. Wallbank, J. R., Patel, A. A., Mucha-Kruczyński, M., Geim, A. K., Fal'ko, V. I. *Phys. Rev. B* **87**, 245408 (2013).
8. Shi, Z. *et al. Nature Phys*. **10**, 743-747 (2014).
9. Tomadin, A., Guinea, F., Polini, M. *Phys. Rev. B* **90**, 161406(R) (2014).
10. Wagner, M. *et al. Nano Lett*. **14**, 894–900 (2014).

11. Bechtel, H. A., Muller, E. A., Olmon, R. L., Martin, M. C., Raschke, M. B. *Proc. Natl. Acad. Sci*. **111**, 7191-7196 (2014).
12. Hermann, P. *et al*., *Opt. Express*. **22**, 17948 (2014).
13. Fehrenbacher, M. *et al. Nano Lett*. **15**, 1057-1061 (2015).
14. Kadic, M. *et al., Nanophotonics*, **1**, 51-64 (2012).
15. Fei, Z. *et al. Nature Nanotechnol*. **8**, 821-825 (2013).
16. Chen, J. *et al. Nano Lett*. **13**, 6210–6215 (2013).
17. Schnell, M., Carney, P. S., Hillenbrand, R. *Nature Commun*. **5**, 3499 (2014).
18. Gerber, J. A., Berweger, S., O'Callahan, B. T., Raschke, M. B. *Phys. Rev. Lett*. **113**, 055502 (2014).